RSC Advances

PAPER

View Article Online
View Journal | View Issue



Cite this: *RSC Adv.*, 2026, **16**, 10720

# Synthesis, structural refinement and luminescence properties of green-emitting $Gd_3GaO_6$:$Tb^{3+}$ phosphors for display applications

Reshu Kajal,[a] Devender Singh, *[a] Rinki Jangra,[a] Pawan Kumar,[a] Varun Kumar,[b] Ramesh Kumar[c] and Harish Kumar[d]

Green-emitting $Tb^{3+}$-doped $Gd_3GaO_6$ phosphors were fabricated through a low-temperature solution-combustion approach utilizing urea as the fuel. Powder XRD analysis suggested an orthorhombic structure with the $Cmc2_1$ space group. Crystallite size was determined using the Scherrer's formula and W–H plot. Surface topography was examined utilizing the FESEM technique, and EDX data confirmed the uniform incorporation of $Tb^{3+}$ ions into the $Gd_3GaO_6$ lattice with proper stoichiometry. A bright green emission was exhibited by phosphors at 543 nm, attributed to the $^5D_4 \rightarrow {}^7F_5$ transition upon irradiation with near ultraviolet light at 272 nm. The observed concentration quenching at 3 mol% $Tb^{3+}$ in the $Gd_3GaO_6$ matrix was attributed to non-radiative energy transfer between the neighbouring $Tb^{3+}$ ions, which became significant at higher doping levels. The quenching observed beyond the optimum concentration is primarily attributed to dipole–dipole interactions between adjacent $Tb^{3+}$ ions. The CIE chromaticity coordinates are located the green region, and the calculated CCT value (4500–5500 K) lies in the cool temperature range, making this phosphor a suitable candidate for cool white-solid state lighting and display devices.

Received 30th September 2025
Accepted 9th February 2026

DOI: 10.1039/d5ra07419c

rsc.li/rsc-advances



## 1. Introduction

In the past decade, inorganic phosphors with tunable luminescent colors have attracted considerable attention owing to their wide applications in bioimaging, color display panels, light-emitting diodes (LEDs), optical thermometry and white light-emitting diodes (w-LEDs).[1–3] Recently, conventional fluorescent and incandescent lamps have been largely replaced by w-LEDs due to their eco-friendly nature, cost-effective production, compactness, high luminescence efficiency, long lifetime, excellent chemical and thermal stability and energy savings of approximately 70% compared with traditional sources.[4,5] For the synthesis of phosphors with desired applications, the suitable choice of a host lattice is very important. Gallates have emerged as promising host lattices for rare-earth ion doping because of their eco-friendly composition, structural stability, excellent optical properties and high resistance to oxygen, acids and bases.[6–9] Rare-earth-doped gallate matrices have thus found applications in waveguides, optical fibers, video displays, smart windows and control panels.[10–13]

In particular, $Gd_3GaO_6$ stands out as an attractive host for phosphor synthesis. It possesses a relatively narrow band gap ($E_g \approx 3.60$ eV) compared with other rare-earth gallates, such as $RE_3GaO_6$ (RE = Nd, Sm, and Eu), enabling efficient absorption and energy transfer. The orthorhombic structure (space group $Cmc2_1$) provides suitable cation sites for rare-earth substitution, and the material exhibits excellent thermal stability with no structural phase transitions over a wide temperature range (298–1273 K) along with favorable thermophysical properties.[14] A key advantage is the presence of $Gd^{3+}$ ions, which can serve as effective sensitizers by transferring energy from their excited $^6P_{7/2}$ state to dopant ions, enhancing luminescence efficiency and overcoming limitations associated with weak direct absorption in the far-UV region.[15,16]

Trivalent lanthanide ions are preferred activators due to their sharp emission bands in the visible region arising from the 4f–4f transitions. By varying the dopant type and concentration, multicolor luminescence can be achieved.[17–19] Among these, the $Tb^{3+}$ ion is a well-established green emitter, primarily due to the magnetic dipole-allowed $^5D_4 \rightarrow {}^7F_5$ transition at ~543 nm, which offers bright green luminescence ideal for w-LEDs, display backlights and optoelectronic devices. $Tb^{3+}$ ions may also show blue emission from the $^5D_4 \rightarrow {}^7F_6$ transition at ~490 nm, but the relative intensity of this component depends on the host crystal field, $Tb^{3+}$ ion concentration and phonon

[a]Department of Chemistry, Maharshi Dayanand University, Rohtak-124001, India. E-mail: devjakhar@gmail.com
[b]Department of Computer Science and Engineering, University Institute of Engineering and Technology (UIET), Maharshi Dayanand University, Rohtak-124001, India
[c]Department of Chemistry, Kurukshetra University, Kurukshetra-136119, Haryana, India
[d]Department of Chemistry, School of Chemical Sciences, Central University of Haryana, Mahendergarh-123031, India

energy, which influence cross-relaxation and non-radiative processes.[20,21] While $Tb^{3+}$-doped phosphors are common in hosts like garnets, silicates or phosphates, many suffer from issues such as thermal quenching, concentration quenching at high doping levels or insufficient color purity due to residual blue emission. Although $Gd_3GaO_6$ has been explored as a host for other activators, primarily $Bi^{3+}$ (for persistent luminescence) and $Er^{3+}$ (for upconversion or color-tunable emission), systematic investigations of $Tb^{3+}$-activated $Gd_3GaO_6$ remain limited or absent in the literature.[22] $Tb^{3+}$ doping in $Gd_3GaO_6$ is interesting due to sensitization by the host $Gd^{3+}$ ion, moderate band gap, low phonon energy and orthorhombic low-symmetry sites could promote intense, high-purity green emission. Such a phosphor could offer advantages for w-LEDs and displays, including better device integration, reduced reabsorption and improved performance under operational conditions.

Traditional solid-state synthesis of inorganic phosphors often involves high-temperature treatments and repeated grinding, which can damage particle surfaces, introduces defects and reduces emission intensity.[23] To address these limitations and produce uniform, high-efficiency nanophosphors, various wet-chemical methods have been developed including sol–gel, microwave-assisted, hydrothermal, precipitation and solution combustion synthesis.[24–27] The solution combustion method is particularly advantageous for $Tb^{3+}$-doped $Gd_3GaO_6$, as it yields homogeneous products with large surface area, high purity, nanoscale morphology and short reaction times.[28] The present work, therefore, focuses on the synthesis of $Tb^{3+}$-doped $Gd_3GaO_6$ nanophosphors *via* solution combustion. The structural and surface properties were characterized using XRD and FESEM, compositional analysis was performed by EDX and photoluminescence properties were investigated at varying dopant concentrations. These results aim to demonstrate the potential of $Gd_3GaO_6$:$Tb^{3+}$ as an intense green-emitting phosphor for solid-state lighting and display applications.

## 2. Experimental

A series of $Gd_{3-x}GaO_6$:$xTb^{3+}$ ($x$ = 1–6 mol%) powdered phosphors was prepared by a facile solution combustion method. The raw materials used for the Gd, Ga and Tb sources were gadolinium nitrate [$Gd(NO_3)_3 \cdot 6H_2O$], gallium nitrate [$Ga(NO_3)_3 \cdot xH_2O$] and terbium nitrate [$Tb(NO3)_3 \cdot 6H_2O$], respectively. The precursors utilized in the solution combustion method were purchased from Sigma-Aldrich. The stoichiometric amount of metal nitrates and urea (organic fuel) was dissolved in a minimum amount of double-distilled water to obtain a homogeneous clear solution. This solution was further heated on a heating plate with uniform stirring and the temperature was maintained at 80 °C to form a gelatinous mixture. The entire solution was transferred to a crucible and placed in a muffle furnace set at 600 °C, where the resulting mixture underwent exothermic reaction, followed by decomposition and evolution of various gases. The crucible was drawn out of the furnace and the obtained voluminous foamy product was manually ground to a fine powder using an agate mortar and pestle. The samples were further calcined in an alumina crucible at 1450 °C for 4 h to improve crystallinity. Final products are brought to ambient temperature, crushed and used for characterizations. The preparation scheme of this method is illustrated in Fig. 1.

## 3. Characterization techniques

Powder X-ray diffraction profiles of the phosphor material were analyzed to determine phase purity by using a Rigaku Ultima-IV X-ray diffractometer equipped with a Cu-Kα source and nickel

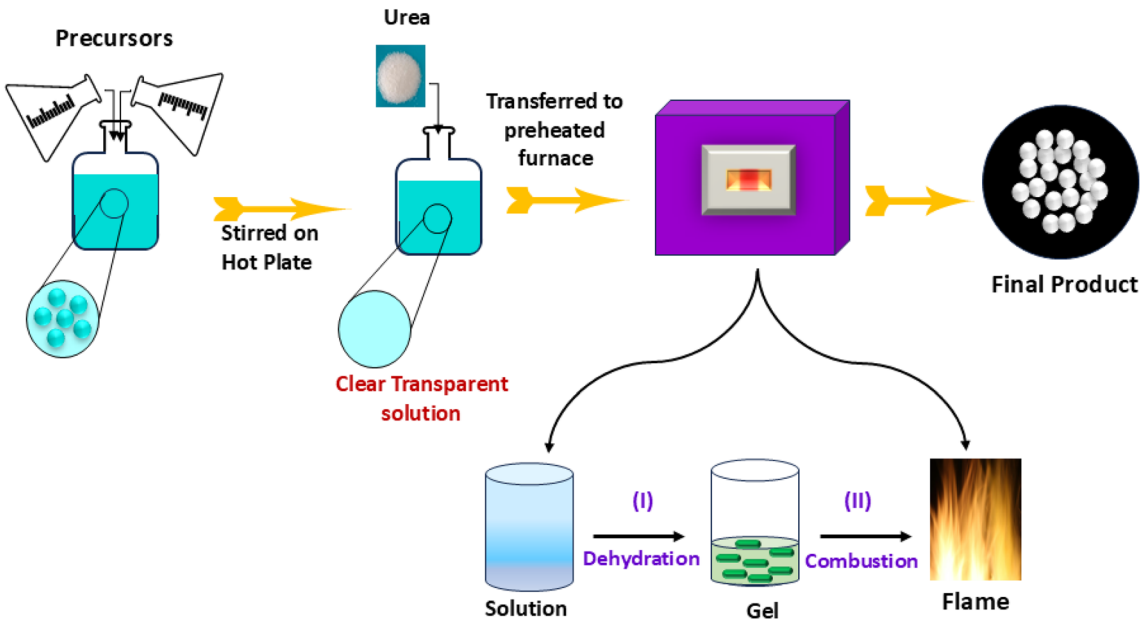


Fig. 1 Representation of the solution combustion synthesis employed in the nanophosphor fabrication.

filter. Scanning was performed between 10°–70°, employing a 0.02° step size and scanning speed of 2° per minute. Microstructural and surface characteristics of the particles were examined by FESEM. The micrographs were taken on a Carl Zeiss Sigma 360 instrument. An Ametek EDX spectrometer was employed for confirming the elemental composition of the sample. Photoluminescence spectral data were recorded on a Horiba-Jobin Fluorolog spectrophotometer using an Xe lamp as an excitation source.

# 4. Results and discussion

## 4.1 XRD measurements

Phase purity and crystallinity of pure and $Tb^{3+}$-doped gadolinium gallium oxide samples were analyzed by means of XRD patterns. Fig. 2(a) shows the diffraction peaks of undoped $Gd_3GaO_6$ and the $Gd_{3-x}GaO_6{:}xTb^{3+}$ ($x$ = 1–6 mol%) phosphors. XRD data confirmed that all peaks were indexed to the orthorhombic phase, consistent with standard JCPDS card number 53–1225, and no additional peaks were present, confirming the non-existence of an impurity phase.[29] Fig. 2(b) shows an enlarged view of diffraction peaks, which revealed peak shifting toward higher $2\theta$ values with increasing $Tb^{3+}$ concentration.

These results were consistent with lattice compression on doping smaller $Tb^{3+}$ ions. Radius difference percentage ($\Delta r$) was evaluated to confirm the replacement of the $Gd^{3+}$ ion with the $Tb^{3+}$ ion by eqn (1).[30]

$$\Delta r = \frac{[R_B(CN) - R_D(CN)]}{R_B(CN)} \times 100\% \quad (1)$$

Here, $R_B(CN)$ = host cation radius, and $R_D(CN)$ = dopant ion radius. The acceptable value of $\Delta r$ for the successful inclusion of a particular cation should be lower than 15%, as reported in the literature.[31] In the present study, the value of $\Delta r$ comes out to be 2% by substituting the radius values for $Gd^{3+}$ ($R_B$ = 1 Å with CN = 7) and $Tb^{3+}$ ($R_D$ = 0.98 Å with CN = 7) ions. This suggests the $Tb^{3+}$ ion successfully replaced the $Gd^{3+}$ ion without altering the crystal structure of the GGO host.

Table 1 XRD peak positions ($2\theta$ values) and corresponding interplanar spacings ($d$-values) of the $Gd_{3-x}GaO_6{:}xTb^{3+}$ ($x$ = 1–6 mol%) phosphors

| Sample | $2\theta$ | $d$-Spacing (Å) |
|---|---|---|
| GGO:0 mol% $Tb^{3+}$ | 30.2062 | 2.9564 |
| GGO:1 mol% $Tb^{3+}$ | 30.2416 | 2.9530 |
| GGO:2 mol% $Tb^{3+}$ | 30.2633 | 2.9509 |
| GGO:3 mol% $Tb^{3+}$ | 30.2952 | 2.9479 |
| GGO:4 mol% $Tb^{3+}$ | 30.3052 | 2.9469 |
| GGO:5 mol% $Tb^{3+}$ | 30.3269 | 2.9449 |
| GGO:6 mol% $Tb^{3+}$ | 30.3491 | 2.9441 |

Furthermore, replacement of a bigger host cation by a smaller $Tb^{3+}$ ion was supported by calculations of interplanar $d$-spacing values determined from the main XRD peak corresponding to various $Tb^{3+}$ doping levels using Bragg's eqn (2).[32]

$$n\lambda = 2d \sin\theta \quad (2)$$

The computed $d$-spacing values are summarized in Table 1. Crystallite size ($D$) was estimated by employing the Debye Scherrer eqn (3) based on XRD broadening.[33]

$$D = \frac{K\lambda}{\beta \cos\theta} \quad (3)$$

In this formula, $\lambda$ represents the wavelength of Cu-K$\alpha$ radiations (1.54 Å), $\beta$ refers to peak broadening (FWHM) and $\theta$ denotes Bragg's angle.

Crystallite size values for the host and $Gd_{3-x}GaO_6{:}xTb^{3+}$ ($x$ = 1–6 mol%) samples were evaluated and are presented in Table 2. Additionally, the Williamson–Hall (W–H) approach was utilized for comprehensive estimation of crystallite size using relation (4).[34]

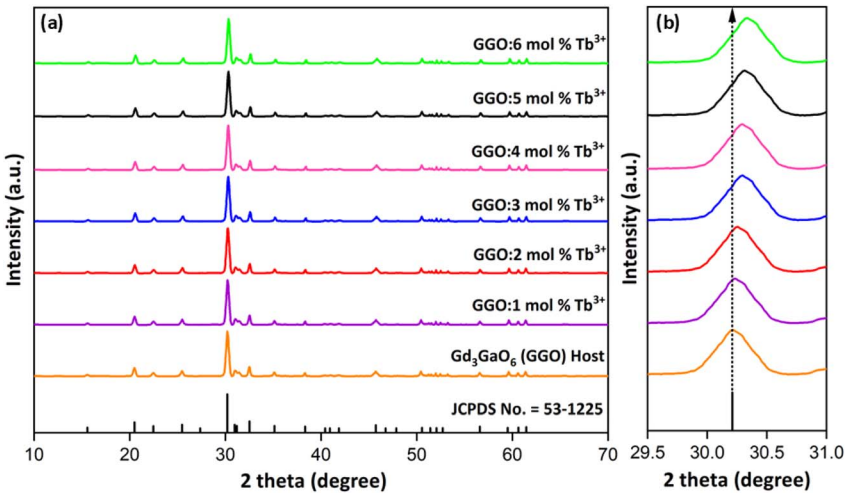


Fig. 2 (a) XRD profiles of $Gd_3GaO_6$ and $Gd_{3-x}GaO_6{:}xTb^{3+}$ ($x$ = 1–6 mol%) and their (b) magnified view, highlighting key features of all the samples.

Table 2 Computed XRD parameters (crystallite size and dislocation density) of the synthesized $Gd_{3-x}GaO6:xTb^{3+}$ ($x$ = 1–6 mol%) phosphors

| Sample (GGO) | $2\theta$ | FWHM | Crystallite size (nm) Scherrer's | W–H | Dislocation density |
|---|---|---|---|---|---|
| GGO:0 mol% $Tb^{3+}$ | 30.2062 | 0.34724 | 24.75 | 41.25 | $1.63 \times 10^{-3}$ |
| GGO:1 mol% $Tb^{3+}$ | 30.2416 | 0.30321 | 28.35 | 43.73 | $1.24 \times 10^{-3}$ |
| GGO:2 mol% $Tb^{3+}$ | 30.2633 | 0.27125 | 31.69 | 46.14 | $9.96 \times 10^{-4}$ |
| GGO:3 mol% $Tb^{3+}$ | 30.2952 | 0.37221 | 23.09 | 38.36 | $1.88 \times 10^{-3}$ |
| GGO:4 mol% $Tb^{3+}$ | 30.3052 | 0.40812 | 21.06 | 35.15 | $2.25 \times 10^{-3}$ |
| GGO:5 mol% $Tb^{3+}$ | 30.3269 | 0.32194 | 26.70 | 42.64 | $1.40 \times 10^{-3}$ |
| GGO:6 mol% $Tb^{3+}$ | 30.3487 | 0.29326 | 29.32 | 44.91 | $1.16 \times 10^{-3}$ |

$$\beta = \frac{K\lambda}{D\cos\theta} + 4\varepsilon \tan\theta \quad (4)$$

This expression can be further modified as eqn (5).[35]

$$\beta\cos\theta = \frac{K\lambda}{D} + 4\varepsilon \sin\theta \quad (5)$$

In this context, $K$ = constant, whose value depends on the shape of particles, $\varepsilon$ = microstrain and all other variables have their common meanings as described earlier. Fig. 3 illustrates a linear fitted W–H plot with 4 sin $\theta$ plotted on the $x$-axis and $\beta$ cos $\theta$ along the $y$-axis.

Crystallite sizes for different doped samples and the host, calculated from the intercept of the linear fitted data, are given in Table 2. Slight variation in crystallite size calculated from Scherrer's formula and W–H plot arises from the assumption of Scherrer's formula, where the strain component was taken as zero and peak broadening is solely attributed to grain size. Dislocation density represented as $\delta$ was also calculated for various samples by employing eqn (6), and values are given in Table 2.[36]

$$\delta = \frac{1}{D^2} \quad (6)$$

### 4.2 Rietveld refinement and crystal structure

To further confirm the single-phase purity of the prepared phosphors, Rietveld refinement analysis was executed. The lattice constraints of representative samples were assessed *via* the FULLPROF software. Fig. 4(a) and (b) represent refinement plots of the undoped GGO host and the optimized $Tb^{3+}$-doped GGO sample, respectively.

The observed and calculated data are shown as black crosses and red/green solid lines, respectively. Vertical (brown) lines represent the Bragg's position and the difference between observed and calculated data is indicated at the bottom by a blue line in each figure. Refinement data for $Gd_3GaO_6$ and $Gd_{3-x}GaO_6:xTb^{3+}$ ($x$ = 3 mol%) are arranged in Table 3. The reliable factors for the GGO host are $R_p = 4.192\%$, $R_{wp} = 5.223\%$ and $\chi^2 = 2.104$ and for $Gd_{2.97}GaO_6$:3 mol% $Tb^{3+}$ sample are $R_p$ = 4.482%, $R_{wp}$ = 5.613% and $\chi^2 = 2.248$. As the reliability factors lie within the 10% range, signifying strong agreement between theoretical and experimental patterns.[37] The measured cell parameters for the optimized sample ($a$ = 8.8742 Å, $b$ = 11.3259 Å, $c$ = 5.4636 Å, $\alpha = \beta = \gamma = 90°$ and $V$ = 549.1371 Å$^3$) are slightly below the standard host values.

This contraction in lattice constraints for $Tb^{3+}$-doped samples is consistent with the substitution of larger $Gd^{3+}$ ions

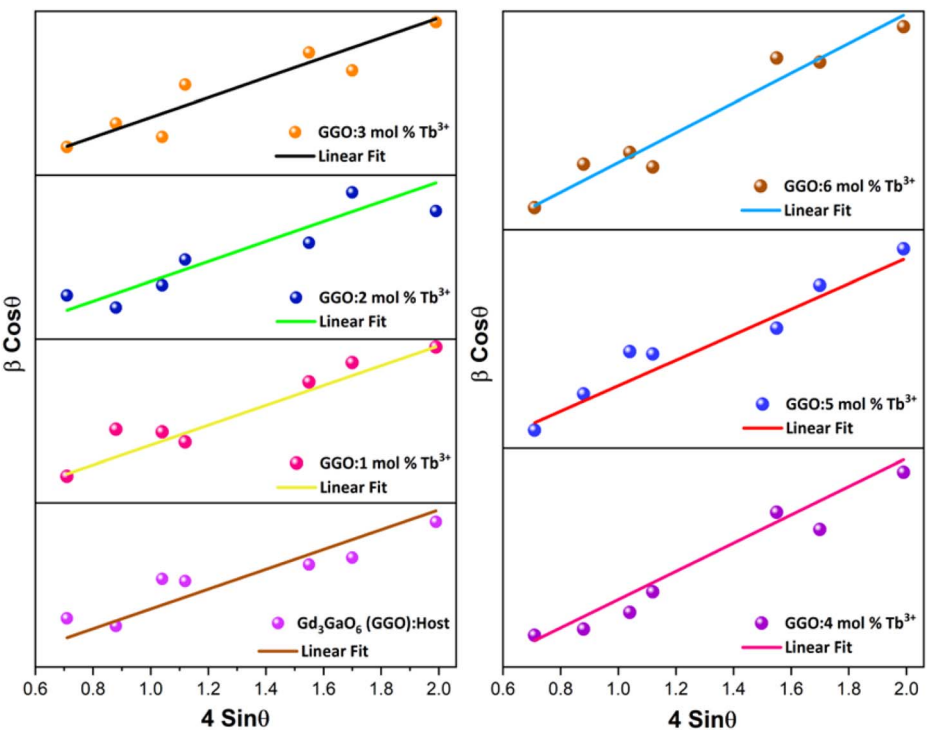


Fig. 3 Williamson–Hall (W–H) plots for the $Gd_3GaO_6$ host and $Gd_{3-x}GaO_6:xTb^{3+}$ ($x$ = 1–6 mol%) phosphors.

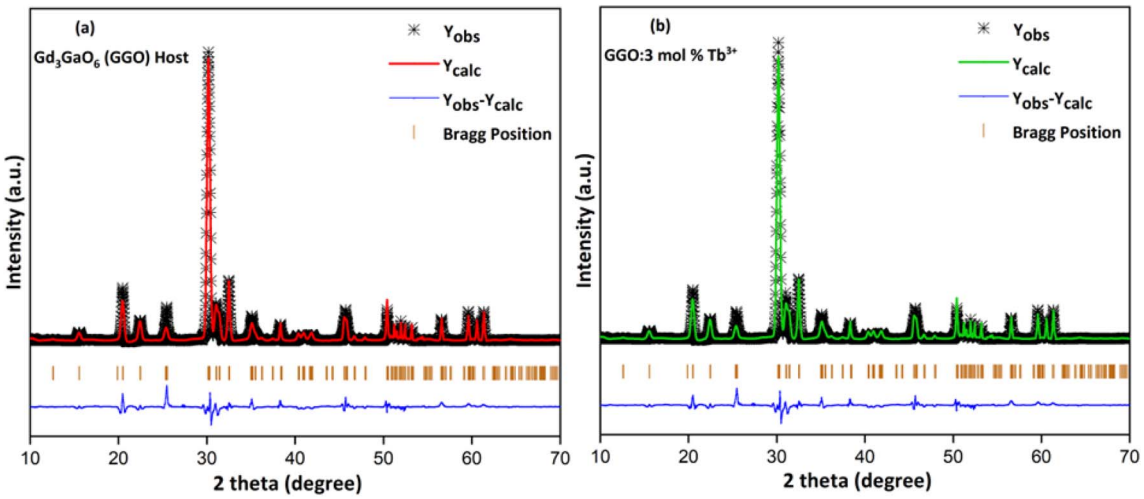


Fig. 4 Rietveld-refined XRD profiles of the (a) $Gd_3GaO_6$ and (b) $Gd_{2.97}GaO_6$:3 mol% $Tb^{3+}$ samples.

by smaller $Tb^{3+}$ ions. The crystal structure of the GGO lattice designed by Vesta software is depicted in Fig. 5. As represented in the structure, there are three different cationic sites: two corresponding to gadolinium [Gd(3) and Gd(4)] and one for gallium [Ga(6)]. [Gd(3), Gd(4) and Ga(6)] ions are located at the 4a, 8b and 4a Wyckoff positions, respectively. Gadolinium ions form the [Gd(3)/(4)$O_7$] polyhedra, in which the Gd(3)/(4) ions are surrounded by seven oxygen atoms, whereas gallium ions form a tetrahedron coordinated to four oxygen atoms. Furthermore, there are four different types of oxygen atoms, *i.e.*, O(1), O(2), O(5) and O(7), located at the 4a, 4b, 4a and 4b crystallographic positions, respectively. Table 4 shows the atomic coordinates ($x$, $y$, $z$) and dislocation factors of the $Gd_3GaO_6$ host.

### 4.3 Morphological insights

To study the structural and surface characteristics of the synthesized phosphor material, FESEM is an essential tool due to its ability to provide structural information at various magnifications. Fig. 6(a) exhibits the FESEM image of the optimized $Gd_{3-x}GaO_6$:$x$$Tb^{3+}$ ($x$ = 3 mol%) sample. The phosphor synthesized *via* the combustion approach demonstrated a porous structure and slight agglomeration, reflecting typical features associated with the exothermic nature of combustion synthesis.

Due to calcination of the sample at a higher temperature, some agglomeration was observed, and the obtained particles are slightly irregular in shape with an average particle size in the 20–50 nm range. Fig. 6(b) depicts the particle size distribution of the optimized sample.

### 4.4 EDX spectral analysis

EDX spectroscopy and elemental mapping of the as-prepared phosphor were conducted in order to ascertain the elemental composition.

Table 3 Rietveld refinement constraints of $Gd_3GaO_6$ (GGO) and the $Gd_{2.97}GaO_6$:3 mol% $Tb^{3+}$ phosphors

| Refinement parameters | Refinement values of $Gd_3GaO_6$ | Refinement values of $Gd_{2.97}GaO_6$:3 mol% $Tb^{3+}$ |
|---|---|---|
| Formula weight | 637.47 | 637.07 |
| Crystal system | Orthorhombic | Orthorhombic |
| 2θ interval | 10–70° | 10–70° |
| Bravais lattice | C | C |
| No. of space group | 36 | 36 |
| Hermann-Mauguin symbol | $Cmc2_1$ | $Cmc2_1$ |
| Hall symbol | C2c-2 | C2c-2 |
| Laue class | mmm | mmm |
| Point group | mm2 | mm2 |
| Lattice symbol | oC | oC |
| Formula unit ($Z$) | 4 | 4 |
| Unit cell parameters | $a$ = 8.9278 Å, $b$ = 11.3859 Å, $c$ = 5.5060 Å<br>$\alpha = \beta = \gamma = 90°$ | $a$ = 8.8742 Å, $b$ = 11.3259 Å, $c$ = 5.4636 Å<br>$\alpha = \beta = \gamma = 90°$ |
| Volume (Å$^3$) | 559.6906 | 549.1371 |
| $R$-Factors | $R_p$ = 4.192%, $R_{wp}$ = 5.223% | $R_p$ = 4.482%, $R_{wp}$ = 5.613% |
| Density (g cm$^{-3}$) | 7.565 | 7.714 |
| $\chi^2$ | 2.104 | 2.248 |

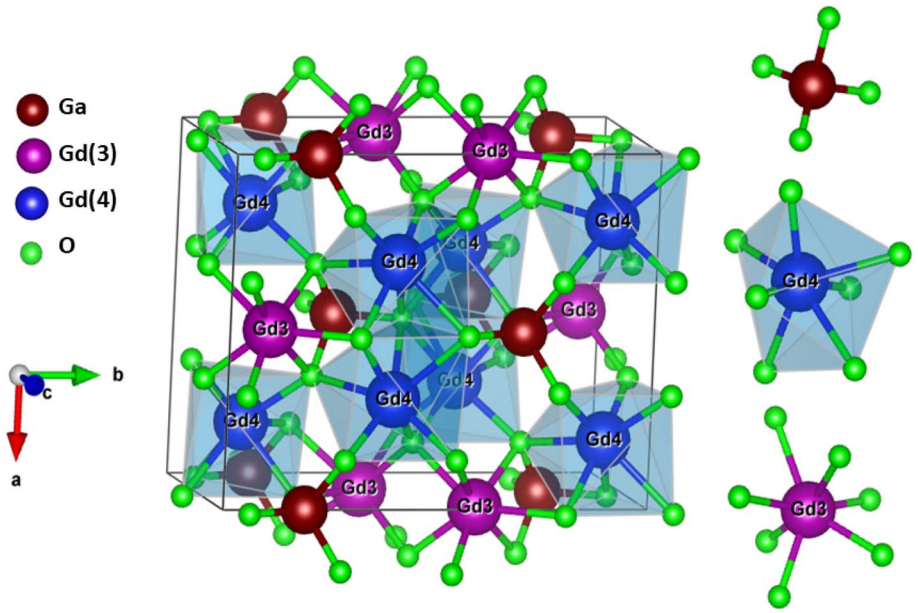


Fig. 5 Visualization of the crystal structure of $Gd_3GaO_6$, illustrating the coordinative environment of individual cations.

Table 4 Crystallographic parameters of the $Gd_3GaO_6$ (GGO) host, exhibiting an orthorhombic crystal system

| Atoms | *x* | *y* | *z* | Occ. | Site | U | Sym. |
|---|---|---|---|---|---|---|---|
| Gd (3) | 0.00000 | 0.39640 | 0.42369 | 1.000 | 4a | 0.205 | m |
| Gd (4) | 0.19300 | 0.10567 | 0.46705 | 1.000 | 8b | 0.205 | 1 |
| O (1) | 0.00000 | 0.04660 | 0.12500 | 1.000 | 4a | 0.205 | m |
| O (2) | 0.00000 | 0.21400 | 0.67100 | 1.000 | 4a | 0.205 | m |
| O (5) | 0.34000 | 0.01890 | 0.20600 | 1.000 | 8b | 0.205 | 1 |
| O (7) | 0.15590 | 0.26010 | 0.17000 | 1.000 | 8b | 0.205 | 1 |
| Ga (6) | 0.00000 | 0.26010 | 0.17000 | 1.000 | 4a | 0.205 | m |

The EDX spectra in Fig. 7(a) provide information about the presence of all expected elements: terbium (Tb), gadolinium (Gd), gallium (Ga) and oxygen (O). The elements are evenly distributed, and no indication of the presence of an extra element was observed in the synthesized sample, suggesting the successful preparation of the $Tb^{3+}$-doped GGO phosphor. The inset of Fig. 7(a), along with the experimental data, illustrates each constituent element together with its atomic and weight percentages. The homogenous distribution of constituent elements was confirmed by X-ray mapping images of the $Gd_{3-x}GaO_6{:}xTb^{3+}$ ($x = 3$ mol%) phosphor (Fig. 7(b)).

### 4.5 Study of photoluminescence behaviour

**4.5.1 Analysis of excitation and emission spectra.** Fig. 8 depicts the photoluminescence excitation spectra of the $Gd_{3-x}GaO_6{:}xTb^{3+}$ ($x = 3$ mol%) sample assessed at an emission wavelength of 545 nm.

The trivalent gadolinium ion exhibits intra-configuration f–f transition $^8S_{7/2} \rightarrow {}^6I_{11/2}$ around 272 nm, which overlaps with the $4f^8 \rightarrow 4f^7 4d^1$ transition of $Tb^{3+}$ ions and is not evidently distinguishable in the spectra.[38,39] There are several other peaks observed in the spectra due to the $4f^n$–$4f^n$ transition of the $Tb^{3+}$ ion, which are assigned to the electronic transitions ($^7F_6 \rightarrow {}^5H_6$) at 306 nm, ($^8S_{7/2} \rightarrow {}^6P_{7/2}$) at 312 nm, ($^7F_6 \rightarrow {}^5L_6$) at 343 nm, ($^7F_6 \rightarrow {}^5L_9$) at 357 nm, ($^7F_6 \rightarrow {}^5G_6$) at 380 nm and ($^7F_6 \rightarrow {}^5D_4$) at 495 nm.[40–42] The emission spectra of varying concentrations of $Tb^{3+}$-doped $Gd_3GaO_6$ phosphors measured at the 272 nm excitation wavelength lie in the range of 450–650 nm and is demonstrated in Fig. 9.

The photoluminescence emission profile is mainly composed of four emission lines due to $^5D_4 \rightarrow {}^7F_3$, $^5D_4 \rightarrow {}^7F_4$, $^5D_4 \rightarrow {}^7F_5$ and $^5D_4 \rightarrow {}^7F_6$ transitions positioned at 626 nm, 590 nm, 543 nm and 490 nm, respectively.[43] Among all the observed transitions, the green emission, originating from the $^5D_4 \rightarrow {}^7F_5$ transition, exhibits the strongest intensity. The transition is distinguished as a magnetic dipole and follows the selection rule $\Delta J = \pm 1$.[44]

The energy level diagram represented in Fig. 10 explains the mechanism of the possibility of energy transfer from $Gd^{3+}$ to the $Tb^{3+}$ ion. Upon UV excitation of $Gd^{3+}$, in the $^6I_{11/2}$ level from the $^8S_{7/2}$ state, the system relaxes to lower-energy levels through non-radiative transitions, eventually populating the $^6P_{7/2}$ energy state. Energy from the $^6P_{7/2}$ excited state of $Gd^{3+}$ may be partially transferred to the $^5H_6$ energy state of $Tb^{3+}$ *via* phonon-assisted dipole–dipole interactions, which then rapidly dissipates to its $^5D_4$ levels, thereby enhancing the luminescence of $Tb^{3+}$. This state subsequently undergoes radiative transition, generating four emission peaks located at 626 nm, 590 nm, 543 nm and 490 nm, corresponding to red, orange-red, green and blue light.

**4.5.2 Concentration quenching.** The emission intensity of phosphor materials is strongly influenced by the concentration of doped ions. Fig. 11 shows the luminescence intensity of the $Gd_3GaO_6$ phosphor at different dopant concentrations of the $Tb^{3+}$ ion. The intensity of peaks in the emission spectrum first increases with an increase in $Tb^{3+}$ ion concentration, reaches

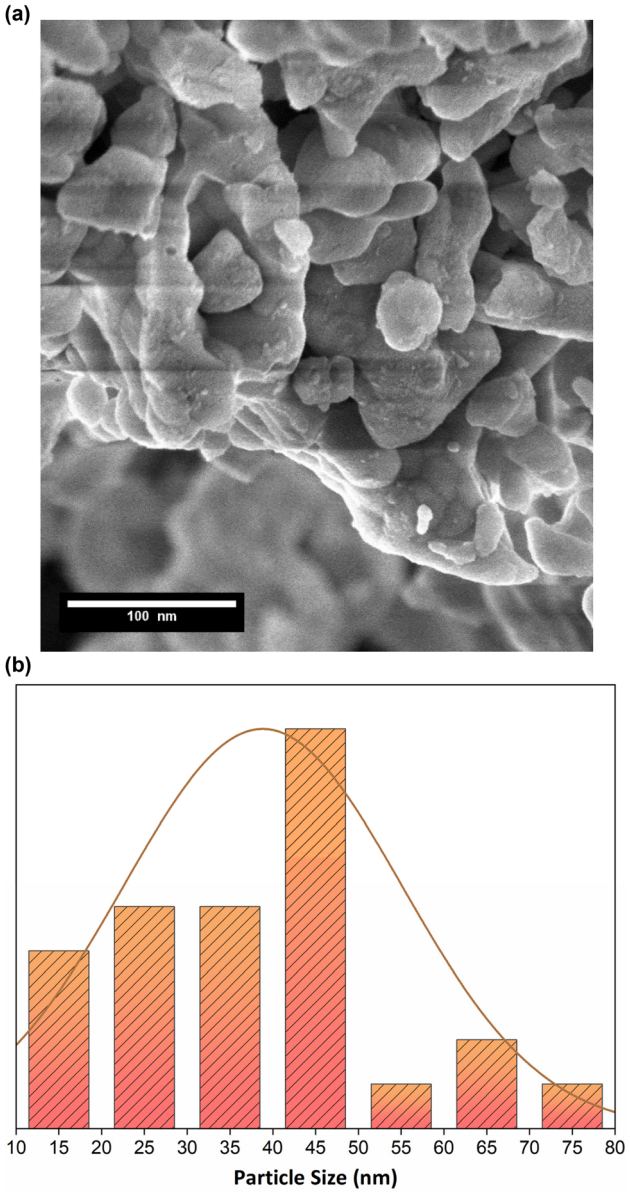


Fig. 6 (a) FESEM image of the $Gd_{3-x}GaO_6$:$xTb^{3+}$ ($x$ = 3 mol%) phosphor, showing its surface morphology. (b) Particle size distribution of the $Gd_{3-x}GaO_6$:$xTb^{3+}$ ($x$ = 3 mol%) sample.

a maximum value at 3 mol% concentration and then decreases on further increasing the concentration of the dopant ion. This decrease is observed owing to the effect of concentration quenching. Thus, according to the above information, 3 mol% was considered the optimized $Tb^{3+}$ ion doping concentration for the $Gd_3GaO_6$ lattice. The concentration quenching phenomenon is generally observed when the activator ion concentration is high, which causes reduced spacing between activator ions, leading to increased non-radiative transitions amongst luminescent centres and results in decreased luminescence intensity.[45] The mechanisms accountable for concentration quenching by non-radiative energy transfer can be radiation absorption, exchange interaction or electrical multipolar interaction.[46]

Due to a lack of significant overlap between the excitation and emission spectra of the $Gd_3GaO_6$:$Tb^{3+}$ phosphor, concentration quenching does not occur *via* the radiation absorption mechanism. Critical distance ($R_c$) between $Tb^{3+}$ ions in the host lattice was used to better understand the exchange interactions. It was calculated by Blasse and Grabmair utilizing the formula given in eqn (7).[47,48]

$$R_c = 2\left(\frac{3V}{4\pi x_c Z}\right)^{\frac{1}{3}} \quad (7)$$

Here, $V$, $Z$ and $x_c$ refer to unit cell volume, number of cations per unit cell and critical concentration of $Tb^{3+}$ ions, respectively. Substituting the values of $Z = 4$, $x_c = 0.03$ and $V = 549.1371$ Å$^3$ for the $Gd_3GaO_6$ system in eqn (7), the estimated $R_c$ appears to be 20.596 Å. According to Van Uitert, exchange interactions are dominant between dopant ions only when the critical distance is close to 5 Å.[49] As the calculated value in the present scenario is beyond the critical limit of 5 Å, interaction *via* the exchange mechanism is less likely to occur. Therefore, multipole–multipole electrostatic interaction is responsible for non-radiative energy transfer. According to Dexter and Schulman's energy transfer theories, concentration quenching of activators is attributed to energy transfer from one dopant ion (donor) to another ion, finally reaching the energy sink within the host lattice. To understand the concentration quenching mechanism of $Gd_3GaO_6$:$Tb^{3+}$ in detail, Dexter's eqn (8) was utilized.[50]

$$\frac{I}{x} = k\left[1 + \beta(x)^{\theta/3}\right]^{-1} \quad (8)$$

In this context, $x$ denotes the dopant ion concentration, $I$ represent the intensity of emission at different $Tb^{3+}$ concentrations, $k$ and $\beta$ are constants and $\theta$ indicates the nature of multipolar interactions. The values of $\theta$ equal to 6, 8 and 10 correspond to dipole–dipole, dipole-quadrupole and quadrupole–quadrupole interactions, respectively. When $\beta(x)^{\theta/3} \gg 1$, eqn (8) can be transformed to eqn (9) as follows.[51,52]

$$\log\left(\frac{I}{x}\right) = -\frac{\theta}{3}\log x + k' \quad (9)$$

Here, $k'$ is a constant. A graph of $\log(I/x)$ *versus* $\log(x)$ was plotted and is represented in Fig. 12.

The relation was found to be almost linear with a slope of −2.17. The computed $\theta$ value is 6.51, which is approximately equal to 6. As a consequence, concentration quenching of the $Gd_3GaO_6$:$Tb^{3+}$ phosphor occurs *via* the electric dipole–dipole interaction mechanism.

### 4.6 Luminescence lifetime

The decay curve of the GGO:$Tb^{3+}$ phosphor at 3 mol% concentration is shown in Fig. 13(a). Measurements were performed using excitation and emission wavelengths of 272 nm and 543 nm, respectively, to obtain the luminescence lifetime.

The decay curve was fitted with various exponential functions, and the best fit was provided by the bi-exponential eqn (10).[53]

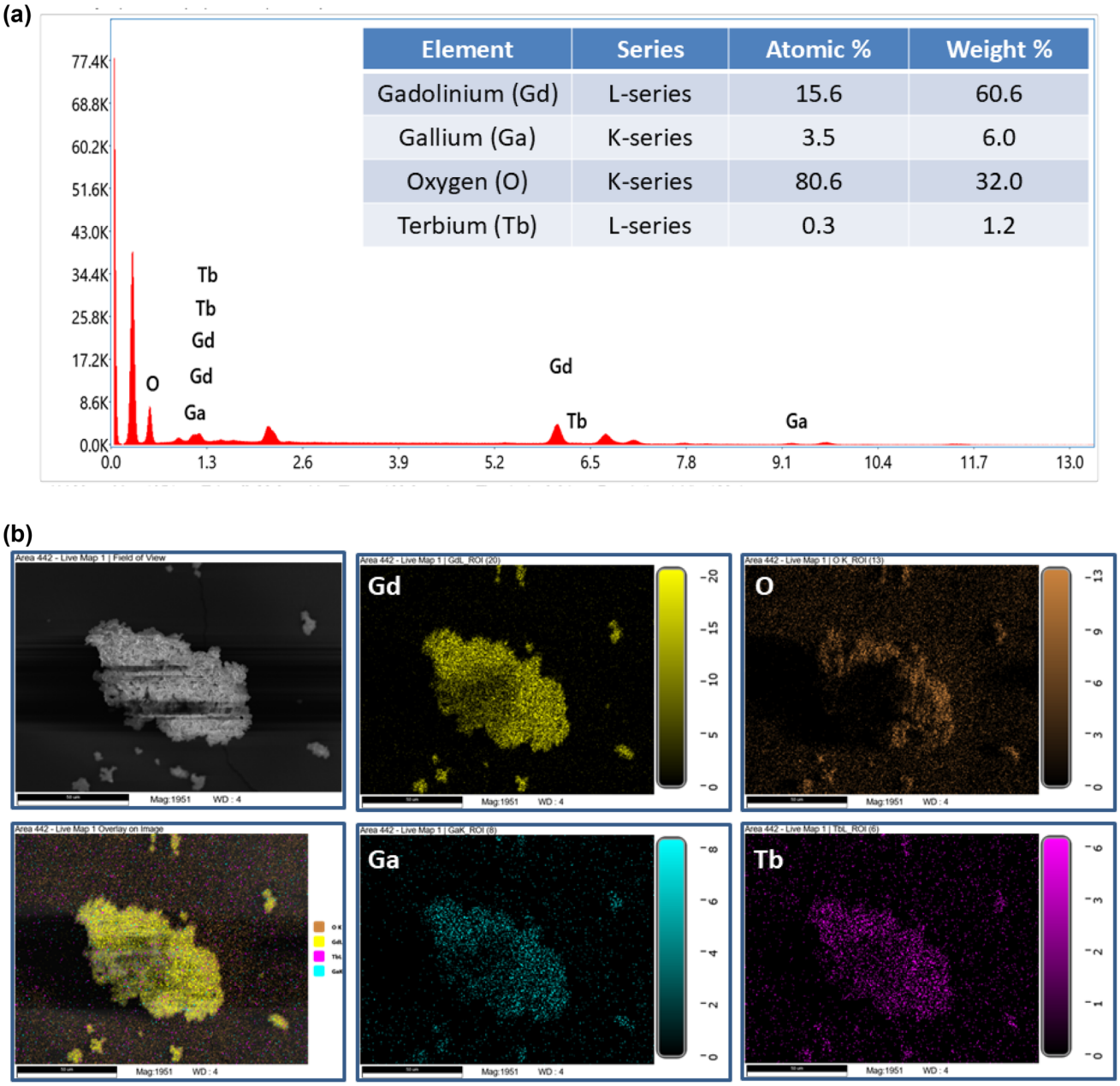


Fig. 7 (a) EDX spectrum of the optimized $Gd_{2.97}GaO_6$:3 mol% $Tb^{3+}$ nanophosphor with an inset table summarizing elemental compositions by atomic % and weight %. (b) EDX mapping images for the $Gd_{2.97}GaO_6$:3 mol% $Tb^{3+}$ nanophosphor, displaying the spatial distribution of the Gd, Ga, Tb and O elements.

$$I_t = I_0 + A_1 \exp\left(-\frac{t}{\tau_1}\right) + A_2 \exp\left(-\frac{t}{\tau_2}\right) \quad (10)$$

In this equation, $\tau_1$ and $\tau_2$ correspond to the fast and slow components, $A_1$ and $A_2$ serve as fitting parameters and $I_t$ and $I_0$ refer to the luminous intensity at time $t$ and $t = 0$, respectively. By substituting the values of $A_1$, $A_2$, $\tau_1$ and $\tau_2$ in eqn (11), the average lifetime can be calculated.[54]

$$\tau_{avg} = \frac{(A_1\tau_1^2 + A_2\tau_2^2)}{(A_1\tau_1 + A_2\tau_2)} \quad (11)$$

The fitted decay analysis reveals the average lifetimes for $G_{3-x}GaO_6$:$xTb^{3+}$ ($x$ = 1–6 mol%) phosphors, which are tabulated in Table 5. The rapid quenching of the average lifetime with increasing $Tb^{3+}$ concentration was attributed to enhanced non-radiative energy transfer processes. Additionally, Auzel's model (Fig. 13(b)) was applied to evaluate radiative lifetimes and interpret luminescence lifetime variations.[55]

$$\tau_C = \frac{\tau_0}{1 + \frac{C}{C_0}e^{-N/3}} \quad (12)$$

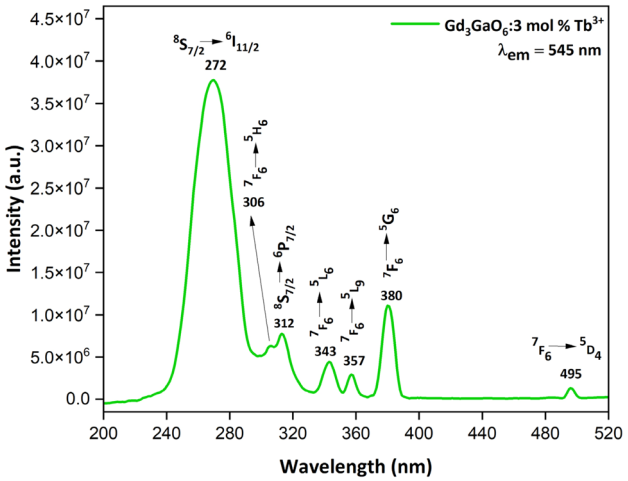


Fig. 8 Excitation spectrum of the $Gd_{2.97}GaO_6$:3 mol% $Tb^{3+}$ phosphor recorded at $\lambda_{em} = 545$ nm.

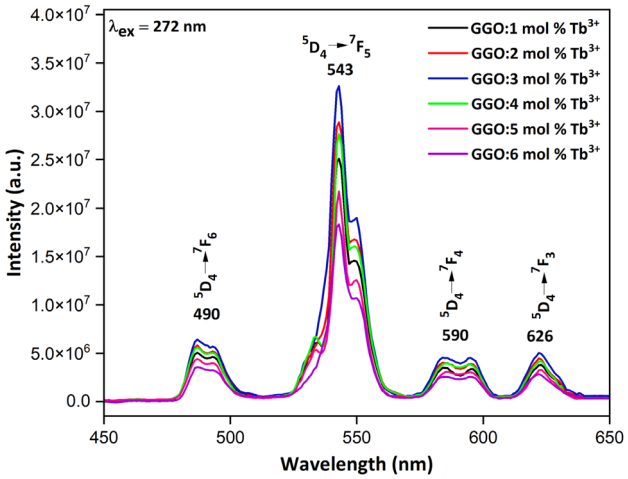


Fig. 9 Emission spectra of the $Gd_{3-x}GaO_6$:$xTb^{3+}$ ($x$ = 1–6 mol%) phosphors.

Here, $\tau_c$ is defined as the lifetime at concentration $C$, $\tau_0$ is the intrinsic radiative lifetime, $C_0$ is a constant and $N$ represents the number of phonons. The intrinsic lifetime was calculated to be 4.86 ms. Furthermore, the quantum efficiencies ($\eta$) of the activated phosphors were calculated using the ratio of the average lifetime to the radiative lifetime (eqn (13)).[56]

$$\eta = \tau_{avg}/\tau_0 \quad (13)$$

The quantum efficiency ($\eta$) values obtained for the synthesized nanophosphors are tabulated in Table 5, and a gradual decrease in the values of quantum efficiencies with increasing $Tb^{3+}$ content was observed owing to non-radiative energy transfer.

### 4.7 Temperature dependent photoluminescence

Thermal stability plays a crucial role in determining the applicability of nanophosphors. Accordingly, the temperature dependent emission spectra of $Gd_{2.97}GaO_6$:3 mol% $Tb^{3+}$ was measured in the temperature range of 298–473 K at intervals of 25 K, as illustrated in Fig. 14(a). The data indicate a steady decrease in luminescence intensity with increasing temperature, which can be attributed to thermal quenching, a phenomenon in which the phosphor's emission intensity diminishes at an elevated temperature range. As illustrated in Fig. 14(b), the emission intensity retains 74.29% of its original value at 473 K relative to the initial temperature, confirming the good thermal stability of the developed phosphor.

To further investigate the thermal quenching behavior of the synthesized material, the activation energy of the optimized GGO:3 mol% phosphor was obtained using the approach given in eqn (14).[57,58]

$$I_T = \frac{I_o}{1 + A\exp\left(-\frac{E_a}{K_B T}\right)} \quad (14)$$

In this expression, $A$ is a constant, $K_B$ represents Boltzmann's constant ($8.617105 \times 10^{-5}$ eV $K^{-1}$) and $I_T$ and $I_0$ correspond to the emission intensities at measured and room temperatures, respectively. Eqn (14) can be modified to eqn (15) as follows.[59,60]

$$\ln\left(\frac{I_o}{I_T} - 1\right) = \ln A - \frac{E_a}{K_B T} \quad (15)$$

The plot of $1/K_BT$ against $\ln(I_0/I_T)$, as shown in Fig. 15, exhibits a linear fit with slope −0.1767 and activation energy of 0.1767 eV, which is consistent with moderate quenching behavior. Table 6 entails a comparison of the $Gd_3GaO_6$:$Tb^{3+}$ phosphor with other well-known $Tb^{3+}$-doped and $Ce^{3+}$-*co*-doped green phosphors in terms of lifetime, quantum efficiency and thermal stability.[61–66]

### 4.8 Colorimetric investigations

To study the color purity and accurate emission color of the synthesized green GGO:$Tb^{3+}$ phosphor, the XY chromaticity coordinate diagram (XY graph) based on CIE 1931 (Commission International de l'Eclairage) was plotted. CIE triangle comprises a triangular area composed of green, red and blue colors and the location of any color within the graph is referred to as its chromaticity point.[67,68] The chromaticity coordinates were evaluated from the photoluminescence emission spectra for different samples of $Tb^{3+}$-doped $Gd_3GaO_6$ phosphors. Fig. 16(a) and (b) represent the CIE color coordinate chart, and the calculated values are summarized in Table 7. It is clearly observed from Fig. 16 that all the coordinates of emitted color lie in the greenish region of the triangle, signifying the single color-emitting property of the GGO:$Tb^{3+}$ phosphor. The obtained CIE chromaticity coordinates ($x$ = 0.3419, $y$ = 0.5962) for the optimized sample are consistent with the $Tb^{3+}$-activated green emission dominated by the $^5D_4 \rightarrow {}^7F_5$ transition (~543 nm) and are comparable to reported $Tb^{3+}$-doped oxides, such as $CsAlSi_2O_6$:$Tb^{3+}$,

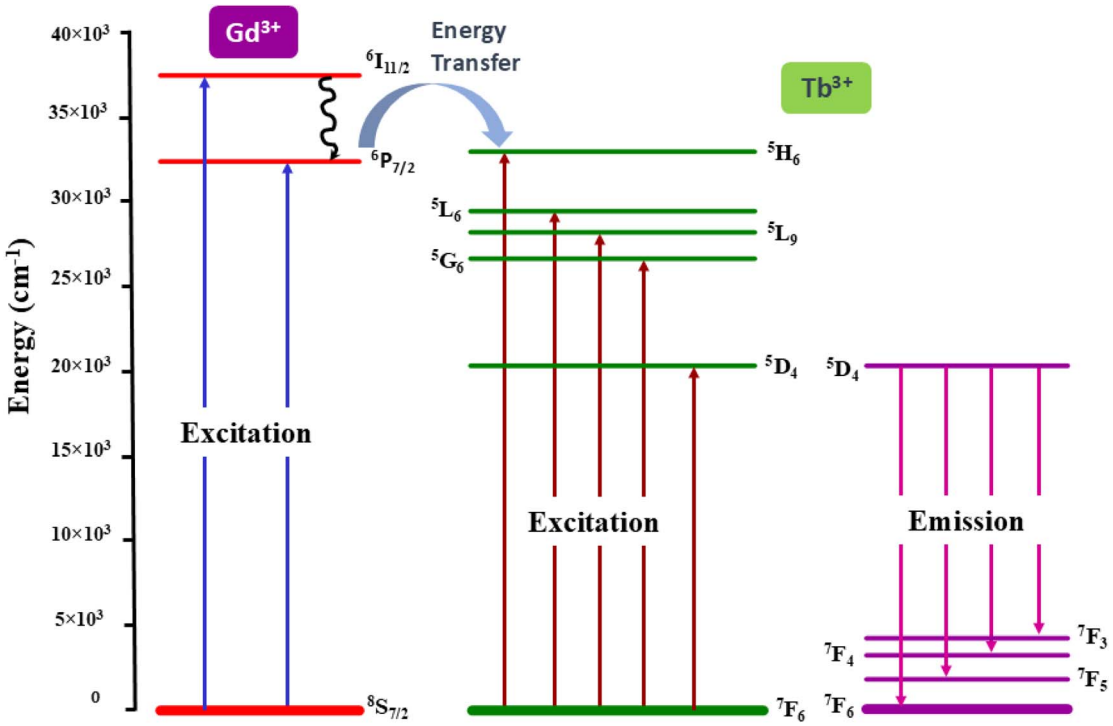


Fig. 10 Depiction of electronic transitions in $Tb^{3+}$ and energy transfer from $Gd^{3+}$ ions under UV excitation.

$Sr_2Ga_2SiO_7$:$Tb^{3+}$ and $MgAl_2O_4$:$Tb^{3+}$.[69–71] CIE 1976 was additionally provided for the validation of luminous characteristics of the prepared samples. According to CIE 1976, the $u'$, $v'$ coordinates (Fig. 17(a) and (b)) are computed by following eqn (16).[72]

$$u' = \frac{4x}{-2x + 12y + 3} \quad v' = \frac{9y}{-2x + 12y + 3} \tag{16}$$

In order to characterize light sources accurately, the color purity of the emitted color was determined using eqn (17).[73]

$$CP = \frac{\sqrt{(x_s - x_i)^2 + (y_s - y_i)^2}}{\sqrt{(x_d - x_i)^2 + (y_d - y_i)^2}} \times 100 \tag{17}$$

In the above equation, $x_s$, $y_s$ represent the CIE coordinates of the sample, $x_i$, $y_i$ correspond to illuminant points and $x_d$, $y_d$ signify chromaticity coordinates of the dominant wavelength. The calculated values of color purity are listed in Table 7, which shows that the color purity of the prepared GGO:3 mol% $Tb^{3+}$ sample is 66.51%. These findings demonstrate the potential use

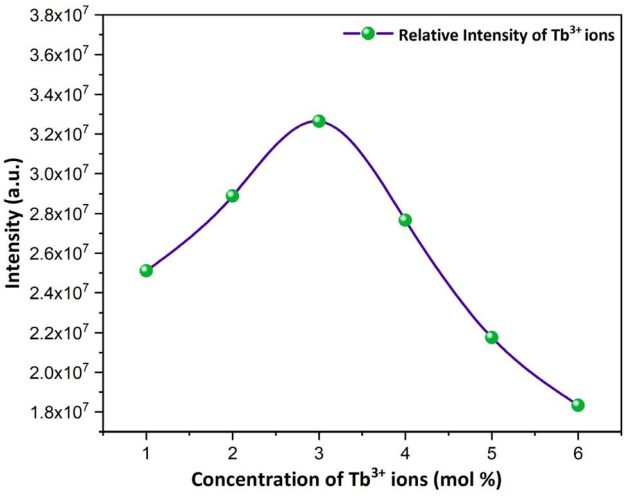


Fig. 11 Emission intensity dependence on $Tb^{3+}$ concentration in the $Gd_{3-x}GaO_6$:$xTb^{3+}$ ($x$ = 1–6 mol%) phosphors.

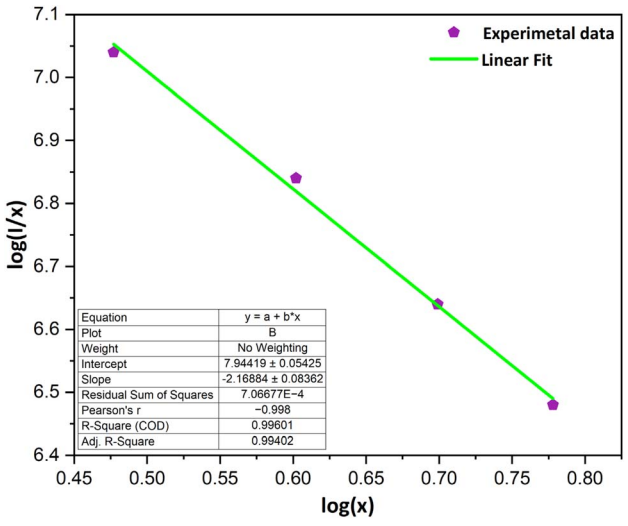


Fig. 12 Graph of the synthesized materials with linear fitting applied after concentration quenching.

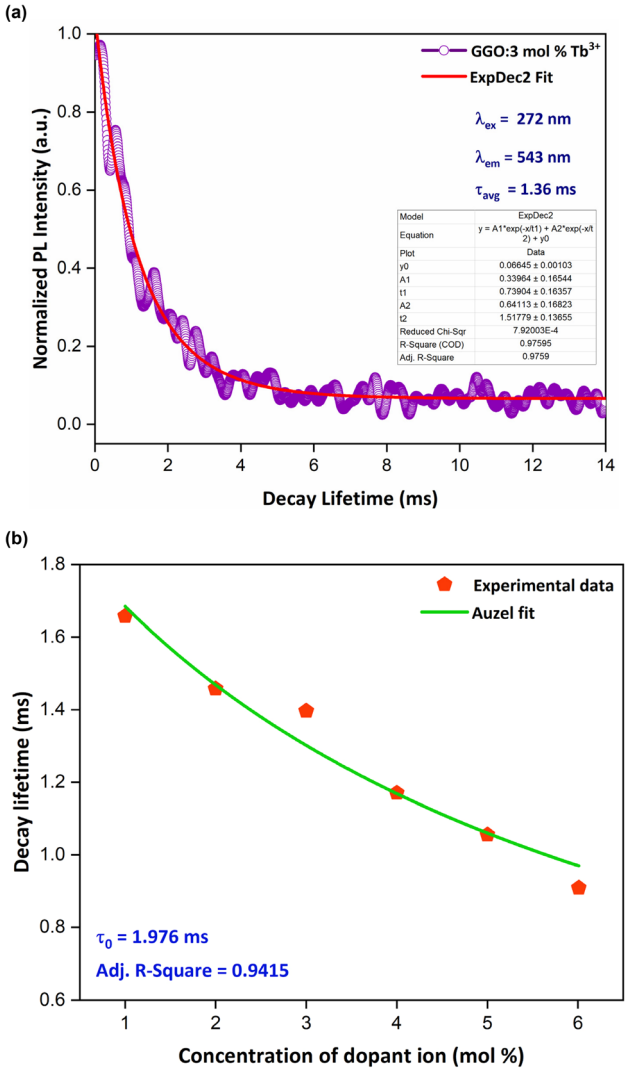


Fig. 13 (a) Decay lifetime curve of the $Gd_{2.97}GaO_6$:3 mol% $Tb^{3+}$ phosphor. (b) Auzel fitting curve of all the prepared samples.

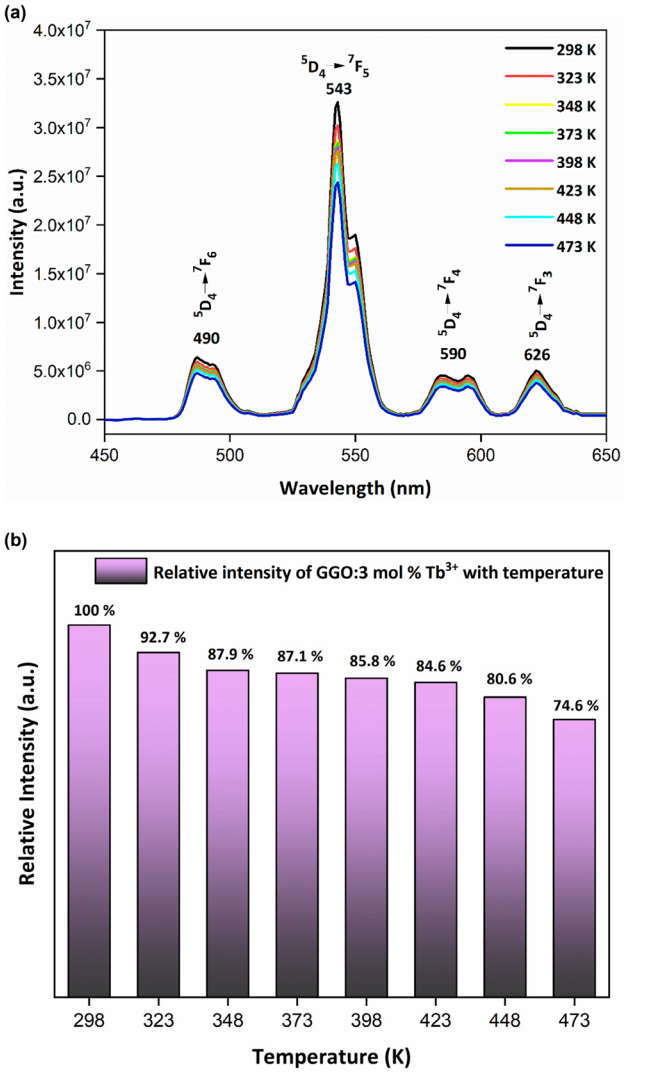


Fig. 14 (a) Temperature-dependent photoluminescence of the $Gd_3GaO_6$:3 mol% $Tb^{3+}$ phosphor. (b) Variations in the relative emission intensity with temperature for the $Gd_{2.97}GaO_6$:3 mol% $Tb^{3+}$ phosphor.

Table 5 Computed decay lifetimes and quantum efficiencies of the $Gd_{3-x}GaO_6$:$xTb^{3+}$ ($x$ = 1–6 mol%) phosphors

| Sample | $\tau_{avg}$ (ms) | $\eta$ (%) |
|---|---|---|
| GGO:1 mol% $Tb^{3+}$ | 1.657 | 83.86 |
| GGO:2 mol% $Tb^{3+}$ | 1.457 | 73.73 |
| GGO:3 mol% $Tb^{3+}$ | 1.396 | 70.65 |
| GGO:4 mol% $Tb^{3+}$ | 1.170 | 59.21 |
| GGO:5 mol% $Tb^{3+}$ | 1.055 | 53.39 |
| GGO:6 mol% $Tb^{3+}$ | 0.909 | 46.00 |

of the $Tb^{3+}$-doped GGO material as an excellent green-emitting phosphor for designing WLEDs and photonic devices. Another key parameter that determines the color quality, along with the temperature characteristics of the light source, is correlated color temperature (CCT). Warm light is generally characterized by CCT values less than 3000 K and values more than 4000 K are associated with cool light.[74]

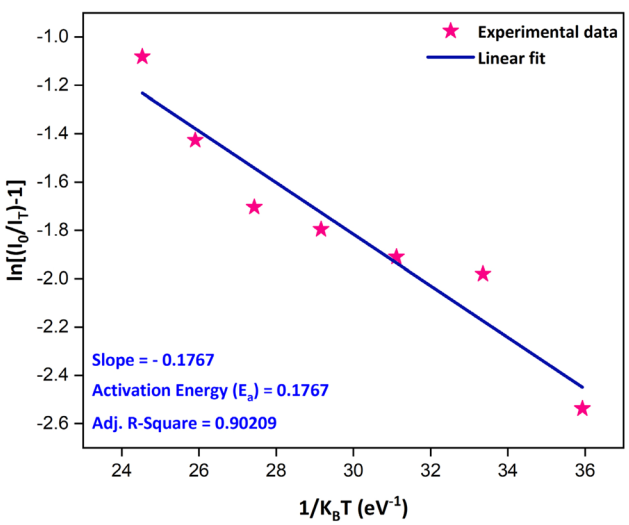


Fig. 15 Linear fit plot for the calculation of activation energy.

Table 6 Comparative optical performance of the synthesized GGO:$Tb^{3+}$ with $Tb^{3+}$-activated phosphors

| Host lattice | Emission peak | Luminescence lifetime | Quantum efficiency | Thermal stability | References |
|---|---|---|---|---|---|
| $Gd_3GaO_6$:$Tb^{3+}$ | 543 nm | 1.396 ms | 70.6% | 74.6% at 473 K | This work |
| $YAl_3(BO_3)_4$:$Tb^{3+}$ | 543 nm | 2.248 ms | — | 70% at 473 K | 61 |
| $Li_2NaBP_2O_8$:$Tb^{3+}$ | 544 nm | 0.440 ms | 34.8% | 89% at 423 K | 62 |
| $SrLaAlO_4$:$Tb^{3+}$ | 548 nm | 1.399 ms | 48% | 61.2% at 398 K | 63 |
| BiOCl:$Tb^{3+}$ | 543 nm | 0.012 ms | — | 24.6% at 423 K | 64 |
| $BaY_4Si_5O_{17}$:$Ce^{3+}$, $Tb^{3+}$ | 544 nm | 20.29 ns | 94.4% | 96.1% at 423 K | 65 |
| $Na_3Sc_2(PO_4)_3$:$Ce^{3+}$, $Tb^{3+}$ | 542 nm | 18.58 ns | 65% | 85.6% at 423 K | 66 |

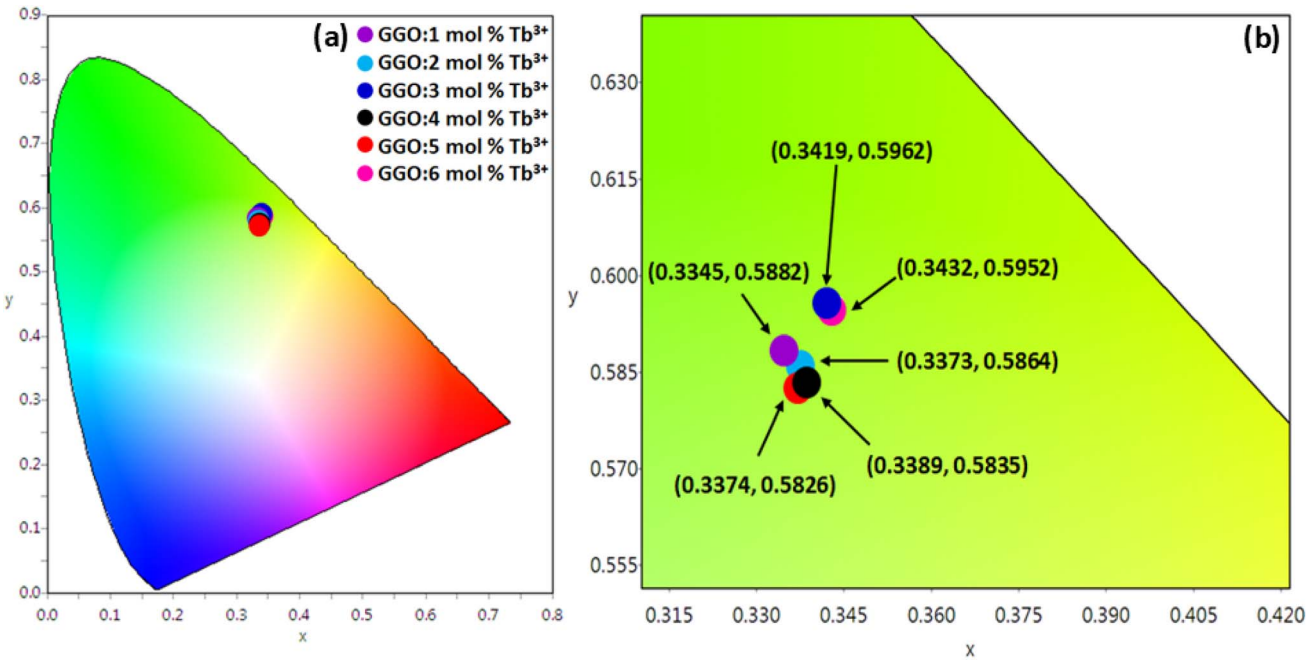


Fig. 16 (a) Representation of chromaticity coordinates ($x$, $y$) plotted on the CIE 1931 diagram. (b) Enlarged view, showing detailed spread of coordinates.

Table 7 CIE ($x$, $y$ and $u'$, $v'$) coordinates, CCT ($K$) and color purity for the GGO:$Tb^{3+}$ phosphors at different $Tb^{3+}$ doping concentrations

| | CIE Co-ordinates | | | | | |
|---|---|---|---|---|---|---|
| Sample | $x$ | $y$ | $u'$ | $v'$ | Color purity (%) | CCT ($K$) |
| GGO:1 mol% $Tb^{3+}$ | 0.3345 | 0.5882 | 0.1425 | 0.5638 | 64.24 | 5471.81 |
| GGO:2 mol% $Tb^{3+}$ | 0.3373 | 0.5864 | 0.1441 | 0.5637 | 63.81 | 5424.37 |
| GGO:3 mol% $Tb^{3+}$ | 0.3419 | 0.5962 | 0.1444 | 0.5666 | 66.51 | 5351.04 |
| GGO:4 mol% $Tb^{3+}$ | 0.3389 | 0.5835 | 0.1454 | 0.5632 | 63.39 | 5395.69 |
| GGO:5 mol% $Tb^{3+}$ | 0.3374 | 0.5826 | 0.1449 | 0.5628 | 63.11 | 4646.13 |
| GGO:6 mol% $Tb^{3+}$ | 0.3432 | 0.5952 | 0.1452 | 0.5665 | 66.30 | 5329.68 |

CCT values for various $Tb^{3+}$-doped samples were calculated by employing the polynomial eqn (18) given by McCamy.[75,76]

$$\mathrm{CCT} = -437n^3 + 3601n^2 - 6861n + 5514.31 \quad (18)$$

$$n = \frac{(x - x_e)}{(y - y_e)} \quad (19)$$

Here, $n$ signifies the anti-slope line connecting $(x, y)$ and $(x_e, y_e)$, and $x_e$ and $y_e$ represent chromaticity epicenters. The CCT values evaluated for all the samples are given in Table 7, which lie in the range of 4600 K–5500 K. The results confirm the cool green light nature of the prepared samples, suggesting their applications for outdoor illumination.

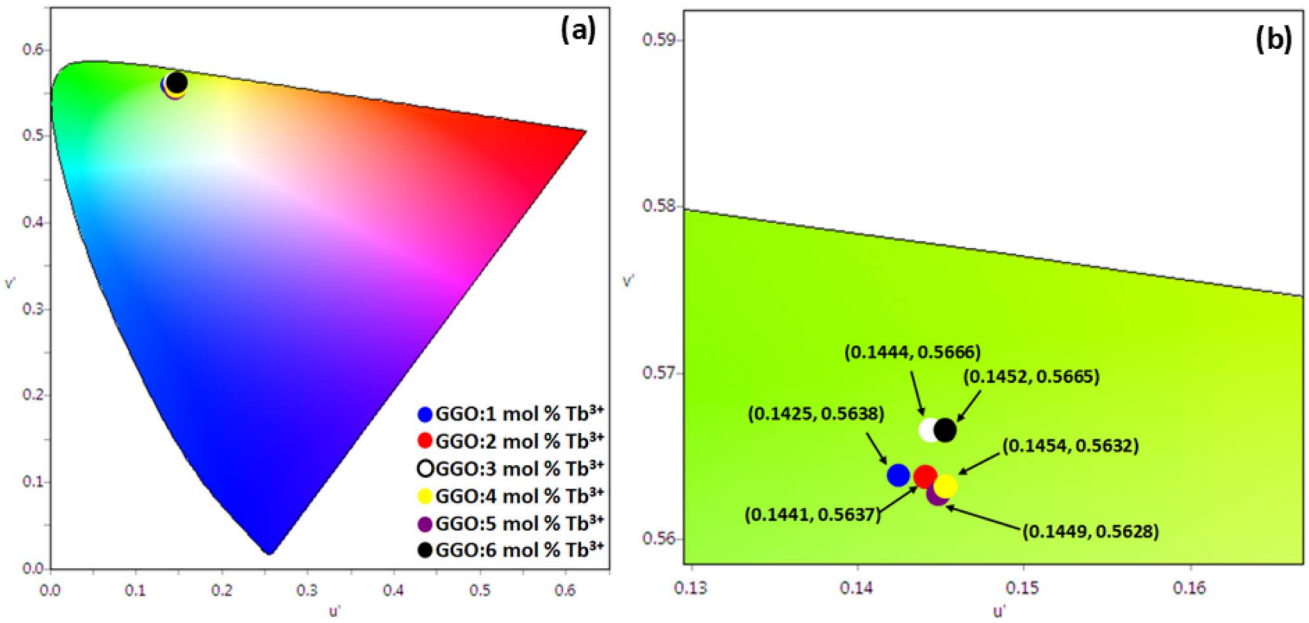


Fig. 17 (a) Representation of chromaticity coordinates ($u'$, $v'$) plotted on the CIE 1976 diagram. (b) Enlarged view, showing detailed spread of coordinates.

## 5. Conclusion

This study includes the synthesis of $Gd_3GaO_6$ phosphors doped with varying concentrations of trivalent terbium *via* an energy-efficient solution combustion approach. Successful inclusion of the $Tb^{3+}$ ion within the $Gd_3GaO_6$ matrix was confirmed by X-ray diffractogram patterns. The GGO:$Tb^{3+}$ phosphors form a crystalline orthorhombic structure belonging to $Cmc2_1$ symmetry as demonstrated by Rietveld refinement analysis. FESEM micrograph, supported by the particle size distribution plot, confirmed that the synthesized phosphor possesses slightly irregular particles having a size in the nano-range (20–50 nm). EDX spectra and mapping provided insights into the distribution of Gd, Ga, O and Tb within the host lattice. Excitation at 272 nm results in multiple emission peaks equivalent to $^5D_4 \rightarrow {}^7F_{3,4,5,6}$, with the strongest being the green emission at 543 nm due to the $^5D_4 \rightarrow {}^7F_5$ electronic transition. The emission intensity increases with the rise in the $Tb^{3+}$ doping concentration, reaching a maximum value at $x = 3$ mol% and then decreases. This decrease in intensity is caused by concentration quenching. Dipole–dipole interactions are the primary reason for the increased transfer of energy between nearby ions, leading to reduced luminescence. In addition, CIE coordinates and CCT values suggest $Gd_3GaO_6$:$Tb^{3+}$ phosphors as efficient green-emitting materials for use in lighting and display technologies.

## Author contributions

Reshu Kajal: data curation, writing – original draft, investigation, methodology; Devender Singh: writing – review & editing, resources, supervision; Rinki Jangra: validation; Pawan Kumar: project administration; Varun Kumar: software; Ramesh Kumar: visualization; Harish Kumar: formal analysis.

## Conflicts of interest

The authors declare that they have no known competing financial interests or personal relationships that could have appeared to influence the work reported in this paper.

## Data availability

Data will be made available on request.

## Acknowledgements

The author (Reshu Kajal) wants to thank University Grants Commission, New Delhi, for providing the Junior Research Fellowship [221610025278].

## References

1 B. M. Manohara, H. Nagabhushana, D. V. Sunitha, K. Thyagarajan, B. D. Prasad, S. C. Sharma, B. M. Nagabhushana and R. P. Chakradhar, *J. Alloys Compd.*, 2014, **592**, 319–327, DOI: 10.1016/j.jallcom.2014.01.003.
2 S. Singh and D. Singh, *J. Mater. Sci.: Mater. Electron.*, 2020, **31**, 5165–5175, DOI: 10.1007/s10854-020-03076-5.
3 R. Kokate, P. Rohilla, S. Kaur, A. S. Rao and V. Singh, *Optik*, 2021, **243**, 167391, DOI: 10.1016/j.ijleo.2021.167391.
4 P. Kumar, S. Singh, I. Gupta, V. Kumar and D. Singh, *J. Mol. Struct.*, 2022, **1265**, 133362, DOI: 10.1016/j.molstruc.2022.133362.

5 S. Cho, J. Kim, D. Hwang and S. W. Cho, *Korean J. Mater. Res.*, 2016, **26**, 67–72, DOI: 10.1016/j.jallcom.2014.07.100.
6 P. Kumar, D. Singh, I. Gupta, S. Singh and V. Kumar, *Chem. Phys. Lett.*, 2023, **812**, 140277, DOI: 10.1016/j.cplett.2022.140277.
7 G. Souadi, Ü. H. Kaynar, M. E. Ayvacikli and N. Can, *Appl. Radiat. Isot.*, 2023, **199**, 110905, DOI: 10.1016/j.apradiso.2023.110905.
8 R. Kajal, D. Singh, R. Jangra, P. Kumar, V. Kumar, H. Kumar and R. Kumar, *J. Alloys Compd.*, 2025, **1050**, 185688, DOI: 10.1016/j.jallcom.2025.185688.
9 T. P. Jyothi, K. Gopal, D. V. Sunitha, D. Kavyashree and A. G. Prakash, *Ceram. Int.*, 2025, **51**(26, Part C), 50644–50657, DOI: 10.1016/j.ceramint.2025.08.293.
10 B. Mari, K. C. Singh, P. Cembrero-Coca, I. Singh, D. Singh and S. Chand, *Displays*, 2013, **34**, 346–351, DOI: 10.1016/j.displa.2013.07.003.
11 I. Gupta, P. Kumar, S. Singh, S. Bhagwan, S. K. Chhikara and D. Singh, *Inorg. Chim. Acta*, 2022, **543**, 121183, DOI: 10.1016/j.ica.2022.121183.
12 S. Raoux, S. Anders, K. M. Yu, I. C. Ivanov and I. G. Brown, *MRS Online Proc. Libr.*, 1995, **392**, 241–246, DOI: 10.1557/PROC-392-241.
13 Y. Gong, L. Li, J. Chen and H. Guo, *Materials*, 2023, **16**, 4711, DOI: 10.1016/j.jallcom.2022.164016.
14 O. N. Kondrat'eva, M. N. Smirnova, G. E. Nikiforova, A. V. Tyurin, V. A. Rassulov and V. A. Ketsko, *J. Alloys Compd.*, 2024, **982**, 173703, DOI: 10.1016/j.jallcom.2024.173703.
15 R. Kajal, R. Jangra, P. Kumar, D. Singh, R. Kumar and H. Kumar, *J. Mol. Struct.*, 2026, **1359**, 145495, DOI: 10.1016/j.molstruc.2026.145495.
16 M. M. Rodríguez-García, J. G. Williams and I. R. Evans, *J. Mater. Chem. C*, 2019, **7**, 7779–7787, DOI: 10.1039/c9tc02336d.
17 I. Gupta, S. Singh, S. Bhagwan and D. Singh, *Ceram. Int.*, 2021, **47**, 19282–19303, DOI: 10.1016/j.ceramint.2021.03.308.
18 J. He, A. A. Haider, H. Jiang, C. Liu, J. Li, W. Qian, J. Zhang and J. Zhu, *Inorg. Chem. Commun.*, 2025, **13**, e01767, DOI: 10.1002/adom.202501767.
19 S. Malik, K. Jakhar, D. Singh, S. Redhu, V. Aggarwal, S. Kumar, R. S. Malik and P. Kumar, *Inorg. Chem. Commun.*, 2025, **181**, 115231, DOI: 10.1016/j.inoche.2025.115231.
20 L. A. Rocha, R. L. Siqueira, J. Esbenshade, M. A. Schiavon and J. L. Ferrari, *J. Alloys Compd.*, 2018, **731**, 889–897, DOI: 10.1016/j.jallcom.2017.10.084.
21 P. Kumar, S. Singh, I. Gupta, V. Kumar and D. Singh, *Optik*, 2022, **267**, 169709, DOI: 10.1016/j.ijleo.2022.169709.
22 Z. Li, Z. Lyu, P. Luo, S. Wei, C. Zhuo, D. Sun, S. Shen and H. You, *Inorg. Chem. Front.*, 2023, **10**, 6746–6753, DOI: 10.1039/D3QI01525D.
23 D. Singh, V. Tanwar, A. P. Simantilleke, B. Mari and P. S. Kadyan, *J. Mater. Sci.:Mater. Electron.*, 2016, **27**, 2260–2266, DOI: 10.1007/s10854-015-4020-1.
24 L. A. Kolahalam, I. K. Viswanath, B. S. Diwakar, B. Govindh, V. Reddy and Y. L. Murthy, *Mater. Today Proc.*, 2019, **18**, 2182–2190, DOI: 10.1016/j.matpr.2019.07.371.
25 S. Singh, D. Singh, P. Siwach, I. Gupta and P. Kumar, *Appl. Res.*, 2025, **4**, e202400190, DOI: 10.1002/appl.202400190.
26 M. Farooq, H. Rafiq and M. H. Rasool, *ECS J. Solid State Sci. Technol.*, 2023, **12**, 126002, DOI: 10.1149/2162-8777/ad1062.
27 D. Singh, S. Sheoran, V. Tanwar and S. Bhagwan, *J. Mater. Sci.:Mater. Electron.*, 2017, **28**, 3243–3253, DOI: 10.1007/s10854-016-5914-2.
28 R. Kajal, D. Singh, R. Jangra, B. Dahiya, M. Kadian, P. Kumar, R. Kumar and H. Kumar, *Opt. Mater.*, 2026, **174**, 117942, DOI: 10.1016/j.optmat.2026.117942.
29 S. Choi, K. Kim, S. Nahm and H. K. Jung, *Opt. Mater.*, 2009, **31**, 1684–1687, DOI: 10.1016/j.optmat.2009.04.007.
30 V. Tanwar, S. Singh, I. Gupta, P. Kumar, H. Kumar, B. Mari and D. Singh, *J. Mol. Struct.*, 2022, **1250**, 131802, DOI: 10.1016/j.molstruc.2021.131802.
31 P. Barik, A. K. Verma, R. Kumar, V. Kumar, P. Dewangan, M. Sahu and I. P. Sahu, *Appl. Phys. A*, 2024, **130**, 391, DOI: 10.1007/s00339-024-07525-4.
32 P. Kumar, S. Singh, I. Gupta, K. Nehra, V. Kumar and D. Singh, *Mater. Chem. Phys.*, 2023, **295**, 127035, DOI: 10.1016/j.matchemphys.2022.127035.
33 T. Ghrib, I. Massoudi, A. L. Al-Otaibi, A. Al-Malki, A. Kharma, E. Al-Hashem, R. A. Al-Ghamdi and R. A. Al-Zuraie, *J. Inorg. Organomet. Polym. Mater.*, 2021, **31**, 239–250, DOI: 10.1007/s10904-020-01761-w.
34 P. Kumar, D. Singh and I. Gupta, *RSC Adv.*, 2023, **13**, 7703–7718, DOI: 10.1039/D3RA00636K.
35 A. S. Rao, *Sens. Actuators, A*, 2024, **372**, 115336, DOI: 10.1016/j.sna.2024.115336.
36 B. M. Manohara, H. Nagabhushana, D. V. Sunitha, K. Thyagarajan, B. D. Prasad, S. C. Sharma, B. M. Nagabhushana and R. P. Chakradhar, *J. Alloys Compd.*, 2014, **592**, 319–327, DOI: 10.1016/j.jallcom.2014.01.003.
37 I. Gupta, D. Singh, S. Singh, P. Kumar, S. Bhagwan and V. Kumar, *Chem. Phys. Lett.*, 2023, **814**, 140350, DOI: 10.1016/j.cplett.2023.140350.
38 R. E. Muenchausen, L. G. Jacobsohn, B. L. Bennett, E. A. McKigney, J. F. Smith, J. A. Valdez and D. W. Cooke, *J. Lumin.*, 2007, **126**, 838–842, DOI: 10.1016/j.jlumin.2006.12.004.
39 P. Kumar, S. Singh, I. Gupta, A. Dalal, V. Kumar and D. Singh, *J. Mater. Sci. Eng. B*, 2023, **288**, 116189, DOI: 10.1016/j.mseb.2022.116189.
40 P. K. Jisha, S. C. Prashantha and H. Nagabhushana, *J. Sci.:Adv. Mater. Devices*, 2017, **2**, 437–444, DOI: 10.1016/j.jsamd.2017.10.001.
41 P. Kumar, D. Singh and H. Kumar, *Mater. Sci. Semicond. Process.*, 2024, **174**, 108162, DOI: 10.1016/j.mssp.2024.108162.
42 I. Gupta, D. Singh, S. Singh, P. Kumar, S. Bhagwan, V. Kumar, H. Kumar and S. K. Chhikara, *Luminescence*, 2023, **38**, 585–599, DOI: 10.1002/bio.4486.

43 M. Ayvacıklı, A. Canimoglu, Y. Ü. Karabulut, Z. Kotan, L. K. Herval, M. P. De Godoy, Y. G. Gobato, M. Henini and N. Can, *J. Alloys Compd.*, 2014, **590**, 417–423, DOI: 10.1016/j.jallcom.2013.12.135.
44 P. Kumar, D. Singh and I. Gupta, *Mater. Res. Bull.*, 2023, **167**, 112413, DOI: 10.1016/j.materresbull.2023.112413.
45 Y. S. Vidya, K. Gurushantha, H. Nagabhushana, S. C. Sharma, K. S. Anantharaju, C. Shivakumara, D. Suresh, H. P. Nagaswarupa, S. C. Prashantha and M. R. Anilkumar, *J. Alloys Compd.*, 2015, **622**, 86–96, DOI: 10.1016/j.jallcom.2014.10.024.
46 Z. C. Wu, J. X. Shi, J. Wang, M. L. Gong and Q. Su, *J. Solid State Chem.*, 2006, **179**, 2356–2360, DOI: 10.1016/j.jssc.2006.04.030.
47 S. Singh and D. Singh, *J. Mater. Sci.: Mater. Electron.*, 2021, **32**, 17674–17685, DOI: 10.1007/s10854-021-06303-9.
48 C. Liu, Y. Wang, R. Li, G. Zhou, A. A. Haider, X. Huang, X. Zhao, Y. Qin, H. Li, H. Jiang and J. Li, *Aggregate*, 2025, **6**, e70125, DOI: 10.1002/agt2.70125.
49 P. Kumar, S. Singh, I. Gupta, V. Kumar and D. Singh, *Luminescence*, 2022, **37**, 1932–1941, DOI: 10.1002/bio.4377.
50 T. A. Safeera and E. I. Anila, *J. Lumin.*, 2019, **205**, 277–281, DOI: 10.1016/j.jlumin.2018.09.033.
51 P. Kumar, D. Singh, I. Gupta, S. Singh, S. Nehra and R. Kumar, *RSC Adv.*, 2023, **13**, 7752–7765, DOI: 10.1039/D3RA00735A.
52 T. T. Chanu and N. R. Singh, *Spectrochim. Acta, Part A Mol. Biomol. Spectrosc.*, 2018, **191**, 539–546, DOI: 10.1016/j.saa.2017.10.060.
53 D. Singh and S. Sheoran, *J. Mater. Sci.:Mater. Electron.*, 2016, **27**, 12707–12718, DOI: 10.1007/s10854-016-5405-5.
54 Z. Li, P. Wang, T. Yang, H. Yu, B. Xiao and M. Zhang, *J. Phys. Chem. C*, 2015, **119**, 27688–27694, DOI: 10.1021/acs.jpcc.5b09328.
55 P. Kumar, D. Singh, S. Singh, H. Kumar and R. Kumar, *RSC Adv.*, 2024, **14**, 18716–18729, DOI: 10.1039/D4RA03833A.
56 M. Luo, X. Sha, B. Chen, X. Zhang, H. Yu, X. Li, J. Zhang, S. Xu, Y. Cao, Y. Wang and X. Wang, *J. Am. Ceram. Soc.*, 2022, **105**, 3353–3363, DOI: 10.1111/jace.18299.
57 P. Kumar, D. Singh and H. Kumar, *RSC Adv.*, 2024, **14**, 755–770, DOI: 10.1039/D3RA07175H.
58 F. L. Joaquim, L. A. Rocha, C. S. Júnior, J. Esbenshade, M. A. Schiavon and J. L. Ferrari, *J. Alloys Compd.*, 2019, **774**, 694–699, DOI: 10.1016/j.jallcom.2018.09.148.
59 P. Kumar, D. Singh and H. Kumar, *Mater. Chem. Phys.*, 2024, **320**, 129418, DOI: 10.1016/j.matchemphys.2024.129418.
60 H. Li, A. A. Haider, Z. Xie, C. Liu, H. Zhang, H. Jiang, J. Li and J. Zhu, *Adv. Sci.*, 2025, **12**, 2415989, DOI: 10.1002/advs.202415989.
61 J. Hakami, Ü. H. Kaynar, M. E. Ayvacikli, M. B. Çoban, J. Garcia-Guinea, P. D. Townsend, M. Oglakci and N. Can, *Ceram. Int.*, 2022, **48**, 32256–32265, DOI: 10.1016/j.ceramint.2022.07.167.
62 J. Zhu, J. Xiang and Y. Mao, *Optik*, 2021, **240**, 166920, DOI: 10.1016/j.ijleo.2021.166920.
63 X. Huang, C. He, X. Wen, Z. Huang, Y. Liu, M. Fang, X. Wu and X. Min, *Opt. Mater.*, 2019, **95**, 109191, DOI: 10.1016/j.optmat.2019.109191.
64 X. Huang, B. Li and H. Guo, *J. Alloys Compd.*, 2017, **695**, 2773–2780, DOI: 10.1016/j.jallcom.2016.11.224.
65 Z. Huang, Z. Lyu, S. Shen, S. Wang, Z. Yang, C. Chen and H. You, *Inorg. Chem.*, 2024, **63**, 6362–6369, DOI: 10.1021/acs.inorgchem.4c00123.
66 H. Guo, B. Devakumar, B. Li and X. Huang, *Dyes Pigm.*, 2018, **151**, 81–88, DOI: 10.1016/j.dyepig.2017.12.051.
67 D. Singh, V. Tanwar, A. P. Samantilleke, B. Mari, S. Bhagwan, P. S. Kadyan and I. Singh, *J. Electron. Mater.*, 2016, **45**, 2718–2724, DOI: 10.1007/s11664-015-4318-z.
68 V. R. Panse, N. S. Kokode, A. Shukla, A. N. Yerpude and S. J. Dhoble, *Optik*, 2016, **127**, 5860–5864, DOI: 10.1016/j.ijleo.2016.04.031.
69 D. Singh, V. Tanwar, S. Bhagwan, P. S. Kadyan and B. Mari, *Adv. Sci. Lett.*, 2014, **20**, 1726–1729, DOI: 10.1166/asl.2014.5736.
70 Z. Liu, S. Wang, Y. Xu, J. Li, Y. Du, J. Hong and Z. Chen, *Appl. Phys. A*, 2025, **131**, 449, DOI: 10.1007/s00339-025-08518-7.
71 S. Zhongxiang, S. Jun, W. Jing, L. Yang and L. Yongfu, *Spectroscopy*, 2023, **38**, 28–34, DOI: 10.56530/spectroscopy.xr3287v2.
72 P. Kumar, D. Singh, S. Kadyan, H. Kumar and R. Kumar, *RSC Adv.*, 2024, **14**, 16560–16573, DOI: 10.1039/D4RA02571G.
73 K. Maheshwari and A. S. Rao, *Opt. Mater.*, 2023, **137**, 113533, DOI: 10.1016/j.optmat.2023.113533.
74 J. Deng, Z. Wang, W. Zhou, M. Yu, J. Min, X. Jiang, Z. Xue, C. Ma, Z. Cheng and G. Luo, *Ceram. Int.*, 2023, **49**, 14478–14486, DOI: 10.1016/j.ceramint.2023.01.036.
75 H. E. Sekrafi, E. Hergli, S. Ferdov, P. J. Coutinho and L. Rebouta, *J. Alloys Compd.*, 2025, **1010**, 177389, DOI: 10.1016/j.jallcom.2024.177389.
76 P. Kumar, D. Singh, I. Gupta, S. Singh, V. Kumar, H. Kumar and S. K. Chhikara, *Inorg. Chem. Commun.*, 2022, **145**, 110064, DOI: 10.1016/j.inoche.2022.110064.